AIAA JOURNAL
Vol. 32, No. 8, August 1994

Application of Essentially Nonoscillatory Schemes to Unsteady Hypersonic Shock-Shock Interference Heating Problems

Xiaolin Zhong*
University of California, Los Angeles, Los Angeles, California 90024

This paper applies the high-order finite-volume essentially nonoscillatory (ENO) schemes to unsteady hypersonic shock-shock interference heating on a circular cylinder. Compared with most of the current second-order numerical methods, which usually are not uniformly accurate, the ENO schemes are able to achieve uniformly high-order accuracy with essentially no oscillation in simulating the aerodynamics of hypersonic flows. Time-accurate high-resolution numerical solutions of the Navier-Stokes equations for a type IV hypersonic shock-wave interference heating problem have been obtained by using the third-order accurate ENO scheme in time and space. The computational results show that the interference-heating flow is inherently unsteady and the inherent unsteadiness is the result of interaction among the unsteady shear layers, impinging jet, and bow shock waves. The numerical results of the surface heating rates and pressure distribution compare well with experimental measurements. Meanwhile, implicit ENO schemes for the Navier-Stokes equations are also tested in supersonic boundary layer and shock/boundary-layer interaction flow computations.

Introduction

Shock-Shock Interference Heating

SHOCK wave interference heating is a critical problem in the development of air-breathing hypersonic vehicles, such as the National Aero-Space Plane (NASP), because extremely high pressures and severe heat-transfer rates can occur in the local interference region on the surface. For example, the local heating rates on the cowl lips of the projected NASP research vehicle caused by the interaction between an impinging shock and cowl-lip bow shock can be orders of magnitude greater than the stagnation values without the interaction. These severely high local heating rates caused by interference heating will be a major concern in the structural design of hypersonic vehicles.

As classified by Edney,[1] there are six different interference heating flow patterns, classed according to the strength of the impinging shock and the location of the intersection point relative to the bow shock. Among these interference patterns, type-IV shock interfence heating creates the most severe pressure and interference heating increases. Figure 1 shows a schematic of a type-IV shock interference heating flowfield, which is created by an oblique shock wave intersecting the nearly normal part of the bow shock. The intersection results in the formation of a supersonic impinging jet, a series of shock waves, expansion waves, and shear layers in a local area of the interaction (shown in Fig. 1). The supersonic impinging jet, which is bounded by two shear layers separating the jet from the upper and lower subsonic regions, impinges on the body surface, and is terminated by a jet bow shock just ahead of the surface. This impinging-jet bow shock wave creates a small stagnation region of high temperature, pressure, and heating rates. Meanwhile, shear layers are formed to separate the supersonic jet from the lower and upper subsonic regions (shown by dotted line in Fig. 1). Many experimental and numerical studies have been done on the shock interference problems.

Recent experimental measurements by Wieting and Holden[2] and Holden[3] have provided detailed results of pressure and heat-transfer-rate distribution on cylinder surfaces for type-III and -IV interference heating at Mach numbers ranging from 6 to 19. In their experiments, it was observed that a significant number of type-IV interactions show intrinsic unsteady oscillation of flow parameters in the jet-impingement regions. Since there is a large aerodynamic load associated with this intrinsic unsteadiness of the flow, the effect of the unsteadiness on the flow parameters, such as maximum heating rates, needs to be understood. Currently, the mechanism of the unsteadiness is unclear. One possibility is that the shock interference flow is inherently unstable.

Many numerical studies of the shock interference heating problems based on the Navier-Stokes equations have been reported. Recent studies include Klopfer and Yee,[4] Thareja et al.,[5] and Gaitonde and Shang.[6] Klopfer and Yee used the second-order implicit total variation diminishing (TVD) schemes to obtain steady-state solutions. In their computations of type-IV interference flow, the convergence rates were slow due to the unsteadiness of the flow, and the impinging shock did not converge to a fixed location but rather tended to oscillate slightly. Thareja et al. used an upwind finite element technique with adaptive triangular grids to compute the interference heating flow. Their computations also experienced

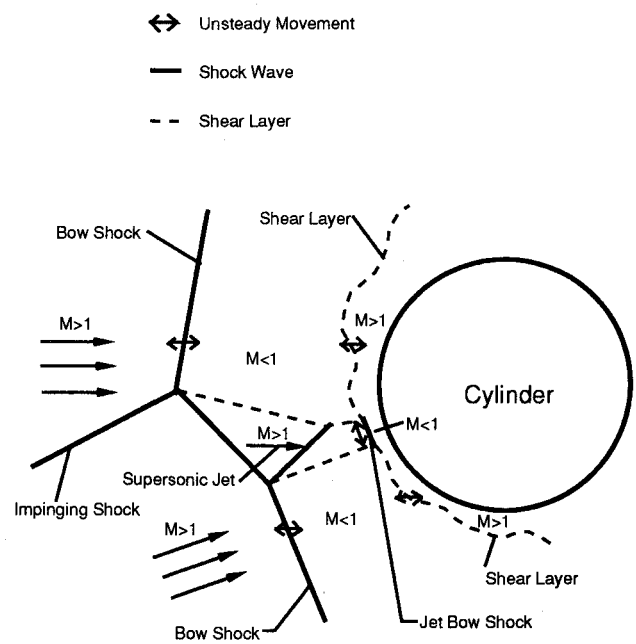

Fig. 1 Schematic of inherently unsteady type-IV shock interference heating on a circular cylinder.

Presented in part as Paper 93-0879 at the AIAA 31st Aerospace Sciences Meeting, Reno, NV, Jan. 11–14, 1993; received May 7, 1993; revision received Oct. 13, 1993; accepted for publication Oct. 14, 1993.

*Assistant Professor, Mechanical, Aerospace, and Nuclear Engineering Department. Member AIAA.

unsteadiness in computing steady-state type-IV interference heating flow. Gaitonde and Shang computed the unsteady flowfield of a type-IV interaction by using an implicit method with a large Courant-Friedrichs-Lewy (CFL) number (= 125). However, the temporal accuracy of their calculations is questionable, because a large CFL number was used in the implicit method which is only first-order accurate in time.

These previous numerical studies have been limited to second-order accuracy. Because the intense shock waves, shear layers, and viscous boundary layer interact in a very small area, high-resolution solutions in the interaction area are crucial to the accurate computation of heat transfer rates. Furthermore, the previous Navier-Stokes solutions obtained by using implicit methods with CFL numbers larger than 1 are not time accurate, and may not be suitable for the unsteady type-IV shock interference heating flow.

Tannehill et al.[7–9] first computed time-accurate shock-on-shock interference heating problems using a time-accurate second-order MacCormack scheme. Because the shear layer and the embedded shock are captured with a relatively coarse set of grids (31×51), some of the detailed structure of the interference flowfield is lost. High-order accurate schemes, such as the essentially nonoscillatory (ENO) schemes, may be especially appropriate for computing the complicated unsteady hypersonic structure of shock interference heating problems.

Essentially Nonoscillatory Schemes

In addition to the physical modeling of the flow, shock-shock interference flow and other complex hypersonic flows around air-breathing hypersonic vehicles require efficient and accurate numerical methods for steady and unsteady flowfield computations. In the numerical computation of these hypersonic flows, the existence of discontinuity surfaces, such as shock waves and shear layers, makes obtaining high-order accurate nonoscillatory solutions difficult. The need for obtaining high-resolution nonoscillatory numerical solutions has led to the development of total variation diminishing (TVD) schemes,[10] which have been successfully used to compute practical flow problems by using the Euler and Navier-Stokes equations. However, the TVD schemes are not uniformly high-order accurate. It is necessary to reduce the accuracy of the schemes to first-order accurate at local extrema of the solutions while maintaining second-order accuracy in other smooth regions.

To avoid the nonuniform accuracy of the TVD schemes, Harten et al.[11] have introduced a class of essentially nonoscillatory (ENO) schemes, which is able to achieve uniformly high-order accuracy. The ENO schemes attempt to avoid the growth of spurious oscillation in numerical solutions by using piecewise polynomial reconstruction based on an adaptive stencil, which is chosen according to the local smoothness of the flow variables to avoid interpolation across discontinuities. The uniformly accurate ENO schemes seem to be more suitable in simulating aerodynamics of hypersonic air-breathing vehicles, compared with current numerical methods for hypersonic flow computations which are not uniformly accurate.

There are several ways to implement the ENO schemes in multidimensions. This paper uses the finite-volume approach presented by Casper[12] who extended the ENO schemes to two-dimensional problems in general curvilinear coordinates. Casper has applied the ENO schemes to two-dimensional boundary value problems for the Euler equations. Since their introduction, the ENO schemes have been applied successfully to solve many one- and two-dimensional Euler equations and Navier-Stokes equations, and recent applications can be found in Refs. 12–16. However, the ENO schemes have not been applied to multidimensional compressible viscous flows with nontrivial geometries and solid walls, which is of practical importance in aerospace applications, and is one of the objectives of this paper.

Objectives

The research in this paper is part of our effort to develop accurateand efficient numerical methods for hypersonic flow at high altitudes in the continuum transition regime. In this paper, we extend the high-order accurate, finite-volume, two-dimensional ENO schemes described by Casper[12] to the Navier-Stokes equations and obtain time-accurate solutions for type-IV shock interference flow. Although the aerothermal heating loads of turbulent flow are important in hypersonic flight at low altitudes, no turbulent modeling is used in the present computations as the main application of the present studies is in high-altitude hypersonic flow where the flow is dominantly laminar.

Our first objective in this paper is to apply high-order accurate implicit and explicit two-dimensional, finite-volume ENO codes to compute the Navier-Stokes equations. The ENO schemes are based on transformed curvilinear coordinates in body-fitted structured grids. The third-order accurate implicit ENO scheme, which is one order more accurate than most of the current methods, is then tested by computing a steady supersonic flow over a boundary layer and a shock/boundary-layer interaction flow.

Our second objective is to study the inherent unsteadiness of the type-IV interference heating problem by obtaining high-order, time-accurate Navier-Stokes solutions. An explicit ENO scheme of third-order accuracy in time and space is used to compute the interference heating flow. The mechanism of the intrinsic unsteadiness of the type-IV interference flow is studied based on the numerical results. Meanwhile, the computed surface pressures and heating rates are compared with those from experimental measurements.

Finite-Volume Essentially Nonoscillatory Schemes for the Navier-Stokes Equations

Finite-Volume Formulations

We use the Cartesian coordinates to demonstrate the numerical methods in the present studies; the extension of the methods in Cartesian coordinates to general curvilinear coordinates is straightforward. The two-dimensional Navier-Stokes equations can be written in the following conservation-law form:

$$\frac{\partial U}{\partial t} + \frac{\partial F}{\partial x} + \frac{\partial G}{\partial y} = 0 \tag{1}$$

where $U = [\rho, \rho u, \rho v, e]^T$, $F = F_e + F_v$, and $G = G_e + G_v$. F_e and G_e are the inviscid flux vectors and F_v and G_v are the viscous flux vectors as follows

$$F_e = \begin{Bmatrix} \rho u \\ \rho u^2 + p \\ \rho uv \\ eu + pu \end{Bmatrix}, \quad G_e = \begin{Bmatrix} \rho u \\ \rho uv \\ \rho v^2 + p \\ ev + pv \end{Bmatrix} \tag{2}$$

and

$$F_v = \begin{Bmatrix} 0 \\ \sigma_{11} \\ \sigma_{12} \\ \sigma_{11}u + \sigma_{12}v + q_1 \end{Bmatrix} \tag{3}$$

$$G_v = \begin{Bmatrix} 0 \\ \sigma_{21} \\ \sigma_{22} \\ \sigma_{22}v + \sigma_{21}u + q_2 \end{Bmatrix} \tag{4}$$

where e denotes the total energy per unit volume ($e = \rho c_v T + \rho (u^2 + v^2)/2$). For the Navier-Stokes equations, the viscous stress and heat flux terms are given by

$$\sigma_{ij} = -\mu \left[\frac{\partial u_i}{\partial x_j} + \frac{\partial u_j}{\partial x_i} - \frac{2}{3}\delta_{ij} \frac{\partial u_k}{\partial x_k} \right] \tag{5}$$

$$q_i = -\kappa \frac{\partial T}{\partial x_i} \tag{6}$$

In the finite-volume approach, the integral form of the conservation equations is obtained by integrating Eq. (1) with respect to x and y over a rectangular grid cell (i, j) in $(x_{i-1/2}, x_{i+1/2}) \times (y_{j-1/2}, y_{j+1/2})$, i.e.,

$$\frac{\partial \bar{\bar{U}}_{ij}}{\partial t} + \frac{1}{A_{ij}} [\tilde{F}_{i+1/2,j} - \tilde{F}_{i-1/2,j} + \tilde{G}_{i,j+1/2} - \tilde{G}_{i,j-1/2}] = 0 \tag{7}$$

where $A_{ij} = \Delta x_i \times \Delta y_j$ is the area of the cell and

$$\bar{\bar{U}}_{ij} + \frac{1}{A_{ij}} \int_{x_{i-1/2}}^{x_{i+1/2}} \int_{y_{j-1/2}}^{y_{j+1/2}} U(x, y, t)\, dy\, dx \tag{8}$$

and

$$\tilde{F}_{i+1/2,j} = \int_{y_{j-1/2}}^{y_{j+1/2}} F(x_{i+1/2}, y, t)\, dy \tag{9}$$

$$\tilde{G}_{i,j+1/2} = \int_{x_{i-1/2}}^{x_{i+1/2}} G(x, y_{j+1/2}, t)\, dx \tag{10}$$

where $\bar{\bar{U}}_{ij}$ is the average of the pointwise value of $U = U(x, y, t)$ in the cell (i, j).

In Eq. (9), surface flux integral $\tilde{F}_{i+1/2,j}$ ($\tilde{G}_{i,j+1/2}$ is evaluated similarly) is computed numerically by using the n-point Gaussian quadrature,

$$\tilde{F}_{i+1/2,j} = \Delta y_j \sum_{k=1}^{n} \omega_k F(x_{i+1/2}, y_j^{(k)}, t) \tag{11}$$

where $(x_{i+1/2}, y_j^{(k)})$ are the nodes of the Gaussian quadrature points along the cell interface at $x = x_{i+1/2}$, and ω_k are the weights. One-point Gaussian quadrature is used for the first- and second-order accurate schemes, and two-point Gaussian quadrature is used for third- and fourth-order accurate schemes.

For the Gaussian quadrature, we need to evaluate the flux term $F = F_e + F_v$ at quadrature points $(x_{i+1/2}, y_j^{(k)})$, where the inviscid flux vector F_e and viscous flux vector F_v are computed by using different methods.

The inviscid term F_e is evaluated by using the Roe approximate Riemann solver[17] based on the values of U_L and U_R, which are obtained by using the ENO reconstruction at the quadrature point $(x_{i+1/2}, y_j^{(k)})$ on the left and right sides of the cell interface $(x = x_{i+1/2})$, respectively, i.e.,

$$F_e = (1/2)[F(U_L) + F(U_R)] - (1/2)|\bar{A}|(U_R - U_L) \tag{12}$$

where $|\bar{A}|$, which is evaluated based on the Roe average of flow variables U_L and U_R, is derived from the diagonalized form of the Jacobian matrix of F_e with all of the eigenvalues replaced by their corresponding absolute values. It has been shown that the Roe scheme may violate the entropy condition and create nonphysical expansion shock when the magnitude of the eigenvalues of matrix $|A|$ is very small. Following Harten,[10] the eigenvalues of $|A|$ are modified to be

$$\lambda = \frac{\lambda^2 + 4\varepsilon^2}{4\varepsilon^2} \quad \text{for } |\lambda| < 2\varepsilon \tag{13}$$

where ε is chosen to be

$$\varepsilon = \tilde{\varepsilon}(u_n + c) \tag{14}$$

where u_n is the normal velocity and c is the speed of sound on cell interface, and $\tilde{\varepsilon}$ is a small constant. In computations of the test cases of this paper, only the case of shock interference heating problem needs modification with $\tilde{\varepsilon} = 0.2$.

The viscous term F_v is evaluated by using the central-difference scheme to approximate the first-order derivatives of velocity and temperature. The central-difference formulas are computed by using the pointwise values of the flow variables at the centroids of grid cells. These pointwise values can also be reconstructed by using the ENO reconstruction. At the present stage of this research, these pointwise values for viscous computations are approximated by the cell averaged values. This approximation of viscous terms is second-order accurate even when the finite-difference formulas are high-order accurate. On the other hand, the inviscid flux approximation used in this paper can be arbitrary order of accuracy, and the accuracy of inviscid flux approximation is most important in capturing the shock interference structures. Research is underway to modify the present viscous schemes so that the schemes are arbitrary high-order accurate for both inviscid and viscous flux computations.

High-Order Accurate One- and Two-Dimensional Essentially Nonoscillatory Reconstruction

The ENO reconstruction of this paper follows the finite-volume ENO reconstruction of Harten et al.[11] and the two-dimensional extension by Casper.[12] Their methods are briefly reviewed as follows. In Eq. (12), reconstruction is needed to obtain the pointwise values of U_L and U_R from the cell average value $\bar{\bar{U}}_{ij}$, which is obtained directly by integrating Eq. (7). Because a fixed-stencil, high-order polynomial interpolation across a discontinuity of the variables leads to oscillatory results, the ENO schemes use adaptive piecewise polynomial interpolation to reconstruct the pointwise values of the variables U_L and U_R. The ENO schemes choose the smoothest interpolation stencils to reconstruct the pointwise value of flow variables, thus avoiding interpolation across discontinuities so that essential nonoscillatory schemes can be achieved with uniformly high-order accuracy in smooth regions of the flowfield.

For a one-dimensional scalar function, we want to reconstruct the point values $w(x)$ of a piecewise smooth function w from its known values of cell average $\bar{w}_i$ defined by

$$\bar{w}_i = \frac{1}{h_i} \int_{x_{i-1/2}}^{x_{i+1/2}} w(\xi)\, d\xi \tag{15}$$

where $h_i = x_{i+1/2} - x_{i-1/2}$. One way to reconstruct $w(x)$ from $\bar{w}_i$ is to interpolate the primitive function $W(x)$ defined by

$$W(x) = \int_{x_{i_0}}^{x} w(\xi)\, d\xi \tag{16}$$

Given the cell average $\bar{w}_i$, the point value of the primitive function $W(x)$ at $x = x_{i+1/2}$ is

$$W_{i+1/2} = \sum_{i=i_0}^{i} \bar{w}_i h_i \tag{17}$$

Because

$$w(x) \equiv \frac{d}{dx} W(x) \tag{18}$$

we obtain a piecewise polynomial interpolation function $H_m(x; W)$ of degree m by interpolating the point values of $W_{i+1/2}$ given by Eq. (17), and then obtain a pointwise approximation to $w(x)$ by

$$R(x; \bar{w}) = \frac{\mathrm{d}}{\mathrm{d}x} H_m(x; W) \tag{19}$$

where $R(x; \bar{w})$ denotes the reconstruction polynomial.

For cell $(x_{i-1/2}, x_{i+1/2})$, we take $H_m(x; W)$ to be the mth-degree polynomial that interpolates the values of $W_{i+1/2}$ at $m+1$ successive points $x_{j+1/2}$ $(j_m \le j \le j_m + m)$, which include $x_{i-1/2}$ and $x_{i+1/2}$. Since there are m different choices of j_m, the interpolation stencil is not unique. The ENO schemes choose a stencil for $(x_{i-1/2}, x_{i+1/2})$ such that $H_m(x; W)$ is smoothest, which is extracted from a table of divided differences of $W(x)$.

The use of adaptive interpolation stencils is the main contribution of the ENO schemes to high-order computations of flow with discontinuity surfaces. However, in smooth regions of the flowfiled, the chattering stencils used in the ENO schemes may cause the schemes to lose accuracy.[18] Shu[19] has demonstrated that this loss of accuracy can be avoided by modifying the ENO schemes through biasing the selection of the stencils in the smooth part of the solutions. Shu's modified ENO schemes will be tested and used in this paper.

Casper[12] extended the preceding one-dimensional ENO reconstruction procedure of Harten et al. to arbitrarily accurate two-dimensional ENO reconstruction via a primitive function. We want to reconstruct the two-dimensional pointwise value of $w(x, y)$ from its cell average $\bar{\bar{w}}_{ij}$. The cell average $\bar{\bar{w}}_{ij}$ defined by Eq. (8) can be written as

$$\bar{\bar{w}}_{ij} = \frac{1}{\Delta x_i} \int_{x_{i-1/2}}^{x_{i+1/2}} \left[\frac{1}{\Delta y_j} \int_{y_{j-1/2}}^{y_{j+1/2}} w(x, y)\, \mathrm{d}y \right] \mathrm{d}x \tag{20}$$

The preceding equation leads to

$$\bar{\bar{w}}_{ij} = \frac{1}{\Delta x_i} \int_{x_{i-1/2}}^{x_{i+1/2}} \bar{w}_j(x)\, \mathrm{d}x \tag{21}$$

where $\bar{w}_j(x)$ is the line average of $w(x, y)$ in y direction in grid cell j, i.e.,

$$\bar{w}_j(x) = \frac{1}{\Delta y_j} \int_{y_{j-1/2}}^{y_{j+1/2}} w(x, y)\, \mathrm{d}y \tag{22}$$

According to Eqs. (21) and (22), we can reconstruct the point value of $w(x, y)$ from cell averages in two steps. First, for each j, Eq. (21) shows that $\bar{\bar{w}}_{ij}$ is the line average in the x direction of the one-dimensional function $\bar{w}_j(x)$ in the cell $(x_{i-1/2}, x_{i+1/2})$. Therefore, the one-dimensional ENO interpolation procedure described earlier can be used in the x direction to obtain the pointwise value of $\bar{w}_j(x)$ from $\bar{\bar{w}}_{ij}$. Then, for a given x, Eq. (22) shows that $\bar{w}_j(x)$ is the line average of $w(x, y)$ in the y direction. Similarly, the one-dimensional ENO interpolation procedure is used in the y direction to obtain the pointwise value of $w(x, y)$ from $\bar{w}_j(x)$, which has been obtained in the first step. An arbitrary order of accuracy can be achieved by using this full two-dimensional ENO interpolation procedure.

It should be pointed out that the preceding procedure is not an extension to two dimensions by simply using two one-dimensional interpolation stencils based on the cell average values. Casper[12] has shown that such dimension-by-dimension two-dimensional ENO schemes are not arbitrary-order accurate and can only achieve second-order accuracy at best.

In the flow region near the shock-shock interaction point in the shock interference flowfields, there may not be enough grid points between two intersection shocks for high-order ENO interpolation. Similar one-dimensional cases exist when two one-dimensional shock waves meet each other.[11] As a result, higher order polynomial interpolation may produce nonphysical negative pressure and density in these local areas. To avoid this problem, the local order of reconstruction in this paper is reduced if the following condition is not met at a cell during the reconstruction process,

$$\left| \frac{p - \bar{p}}{\bar{p}} \right| \le 0.8 \quad \text{and} \quad \left| \frac{\rho - \bar{\rho}}{\bar{\rho}} \right| \le 0.8 \tag{23}$$

where $\bar{p}$ and $\bar{\rho}$ are the cell average pressure and density, and p and ρ are point values obtained by ENO reconstruction within the same cell. This local order reduction is done only in the local one or two cell points near the triple shock-intersecting point, and this order reduction does not affect the overall accuracy of the resolutions in the smooth region.

Explicit and Implicit Time-Stepping Schemes

Equation (7), which represents a system of ordinary differential equations, is solved by using time-stepping schemes. For time-accurate computations, we use the explicit TVD Runge-Kutta time-stepping schemes of Shu and Osher[20] to compute the flow problems.

On the other hand, for steady viscous flow simulations, the grid size across the boundary layer near body surfaces is so small that the use of implicit methods will greatly reduce the computer time in the simulations. Therefore, Eq. (7) is integrated by the implicit line Gauss-Seidel relaxation method described by MacCormack[21] so that large CFL numbers can be used to obtain fast convergence to steady-state solutions. The implicit equations in the delta form are used so that the implicit part of the equations can be computed by using the modified version of the Steger-Warming flux splitting method,[21] which can achieve fast convergence for implicit methods.

General Curvilinear Coordinates

The two-dimensional ENO schemes used to solve the Navier-Stokes equations in this paper are based on transformed curvilinear coordinates in structured body-fitted grids. The use of the structured grids makes the arbitrary-order, two-dimensional ENO reconstruction more efficient compared with using unstructured grids. In the general curvilinear coordinates, the conservation equations in Cartesian coordinates are transformed in the curvilinear coordinates (ξ, η) in conservation-law form. The ENO construction procedures are extended to (ξ, η) space similar to the procedures in the Cartesian coordinates described earlier. The details can be found in Ref. 12.

Boundary Conditions

A nonslip boundary condition is used on the wall surface. The flow variables on the wall are obtained by using one-sided polynomial interpolations. The flow variables in the supersonic freestream are specified to the given freestream values. The computational domain is chosen such that the flow outside the boundary layer is supersonic at the exit. Therefore, the flow variables at the exit boundaries are computed by using linear extrapolation. Because a large reconstruction stencil is needed for high-order ENO interpolation, the adaptive interpolation stencil in the interior grid cells near the boundaries is chosen such that only interior flow variables are involved in the interpolations.

Test Cases for Essentially Nonoscillatory Schemes

The performance of the two-dimensional, finite-volume ENO schemes in solving the Navier-Stokes equations is tested by computing two test cases of supersonic boundary layer and shock/boundary-layer interaction flows. The test cases are computed by

using five different test runs of the ENO schemes with spatial accuracy ranging from first- to third-order accurate, with and without Shu's modification. The results of these test cases are compared with one another to evaluate the effect of the increasing order of accuracy in the ENO schemes.

The accuracy of the high-order finite-volume ENO reconstruction has been studied by Casper.[22] Because we follow the same reconstruction procedure as Casper, we do not repeat the accuracy studies in this paper. The test cases of this paper serve mainly as validation tests for our newly developed, finite-volume ENO codes for the Navier-Stokes equations.

Supersonic Boundary Layer

The first test case is a supersonic laminar flow over a flat plate. The freestream flow conditions are: $M_\infty = 2.0$, $Re_\infty/L = 1.65 \times 10^6$/m, $T_\infty = T_{wall} = 221.6$ K, and $L = 1.83$ m. The viscosity coefficient is computed according to Sutherland's Law for air, $Pr = 0.72$, and $\gamma = 1.4$. The results of the two-dimensional ENO schemes for the Navier-Stokes equations are compared with the results of boundary-layer computations presented in Ref. 23.

A coarse grid consisting of 20×20 uniformly spaced cells in both the x and y directions is used to compute the boundary-layer flow. The velocity and temperature profiles across the boundary layer at $x = 0.915$ m are plotted to compare with the results obtained from the boundary-layer theory. The numerical accuracy of the present computational results are also evaluated by comparison with fine-grid solutions obtained by using 40×40 uniform grids with the second-order ENO scheme.

The velocity and temperature profiles across the supersonic boundary layer at $x = 0.915$ m are shown in Fig. 2. The boundary-layer-theory and fine-grid solutions are used as the basis of comparisons. Comparison of the results in the figure shows that as the order of accuracy of the ENO schemes increases, the accuracy of

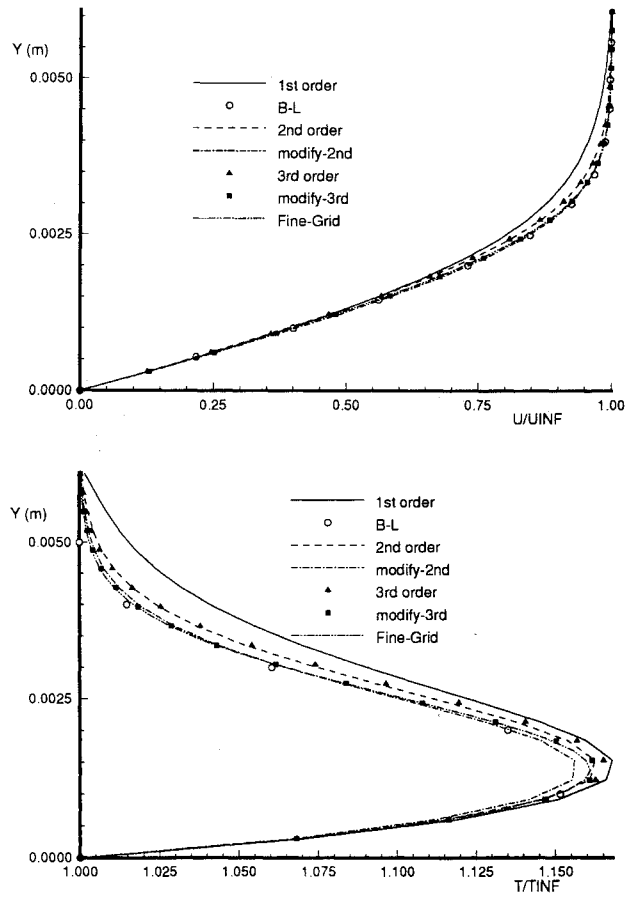

Fig. 2 Velocity and temperature profiles across supersonic boundary layer ($M_\infty = 2$); ENO schemes of first–third orders with and without Shu's modification are compared with the boundary-layer theory and 40×40 fine-grid solutions.

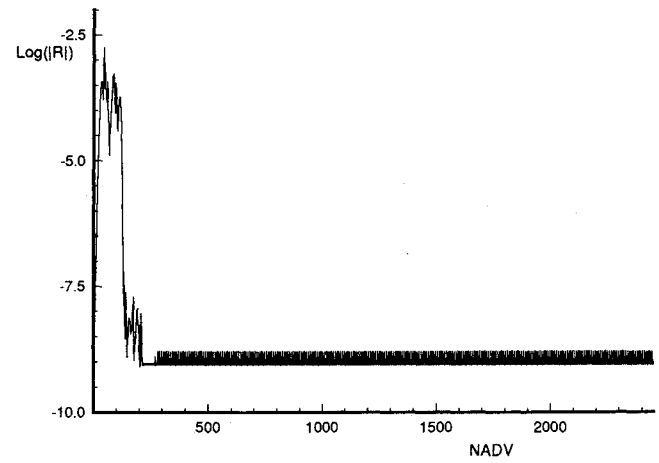

Fig. 3 Convergence history of iteration residuals in computing steady-state solutions by the implicit, third-order ENO schemes for supersonic boundary-layer-flow computations ($M_\infty = 2$).

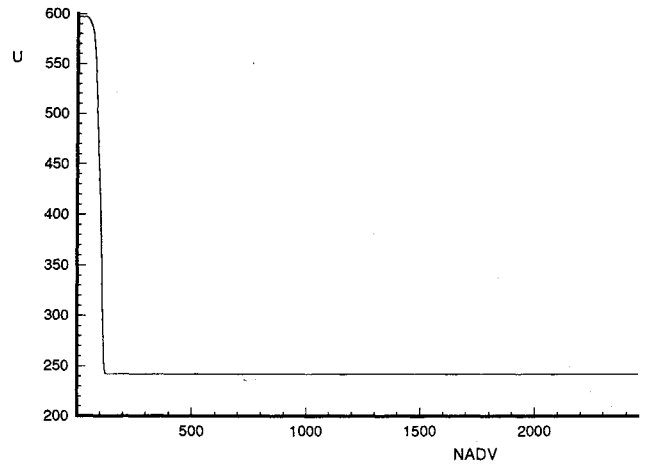

Fig. 4 Computational convergence history of the x component of the velocity vector at a fixed location in the flowfield near the wall surface for supersonic boundary-layer-flow computations ($M_\infty = 2$).

both the velocity and temperature profiles improves. Compared with boundary-layer-theory and fine-grid solutions, Shu's modified ENO schemes are more accurate compared with the corresponding ENO schemes of the same order without modification. However, the computations that used the modified ENO schemes show more fluctuation in the convergence process compared with the ENO schemes. The results of the second-order and third-order ENO schemes are very close except in the shoulder area of the temperature profile. This may be due to the fact that there is no shock wave in the boundary-layer flow and the viscous terms are not yet fully third-order accurate in the codes.

The figure also shows that the coarse-grid results of the third-order modified ENO scheme agree very well with the fine-grid solutions. The numerical error of the coarse-grid solutions can be considered bounded by the difference between themselves and the fine-grid solutions.

Because the ENO schemes use chattering interpolation stencils, the convergence to steady-state solutions is a major concern in applying the ENO schemes to steady flow computations. The convergence history of iteration residuals, $\log |R^{(n)}|$, in computing steady-state solutions of the present case by the implicit second-order ENO schemes is shown in Fig. 3, where $|R^{(n)}|$ is the maximum variation (residuals) of the flow-variable vector U at iteration step n, i.e.,

$$|R^{(n)}| = \max_{ij} \left| \frac{U_{ij}^{(n)} - U_{ij}^{(n-1)}}{U_\infty} \right| \tag{24}$$

Because the reconstruction stencils in the ENO reconstruction are determined by local smoothness of the variables at each time step, the stencils are not fixed in the computations. Consequently, the residuals for the ENO schemes do not converge to machine zero. Figure 3 shows that the computational residuals approach finite values after several hundred steps. As a result, the steady-state solutions have slight oscillations. However, as long as a given oscillation is within the limit of numerical error, the solutions can be considered steady-state solutions. This argument is supported by Fig. 4, which shows the computational convergence history of the x component of the velocity vector at a fixed location in the flowfield near the wall surface in the same computation. The figure shows that though the residuals cannot converge to machine zero, the actual values of the flow variables only have slight variations after the computation is considered to be converged.

Shock-Wave/Boundary-Layer Interaction

The second test case is the interaction of an oblique shock wave with a laminar boundary layer. Figure 5, which is taken from Ref. 25, shows the sketch of a flowfield with shock-wave/boundary-layer interaction. The impinging oblique shock incident upon the boundary layer on the flat plate is chosen to be strong enough to cause the boundary layer to separate from the surface and reattach downstream. The problem has been studied experimentally by Hakkinen et al.[24] at the following freestream flow conditions: $M_\infty = 2.0$, $Re_\infty = 2.96\times10^5$, and the incident shock wave is imposed such that the shock intersects the flat plate at 32.6 deg. The Reynolds number is based on the reference length measured from the leading edge to the intersection point. The same problem has been studied numerically by many researchers.[25,26]

In this paper, the five test runs of the ENO schemes with first- to third-order spatial accuracy are used to compute the flowfield. The results of the first-, second-, and third-order ENO schemes with Shu's modification are shown in this paper. The results presented here are computational results using a 102×144 grid above the plate surface. A set of uniformly spaced grids is used in the x direction and exponentially stretched grids are used in the y direction. The implicit ENO schemes using the Roe approximate Riemann solver without entropy correction are used in the computations. The CFL number for typical run is 5×10^5. Each run takes about 200 iterations until the residuals of the iterations converge to a fix pattern.

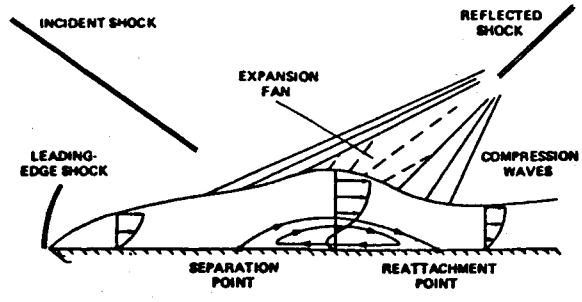

Fig. 5 Sketch of the flowfield of shock/boundary-layer interaction.

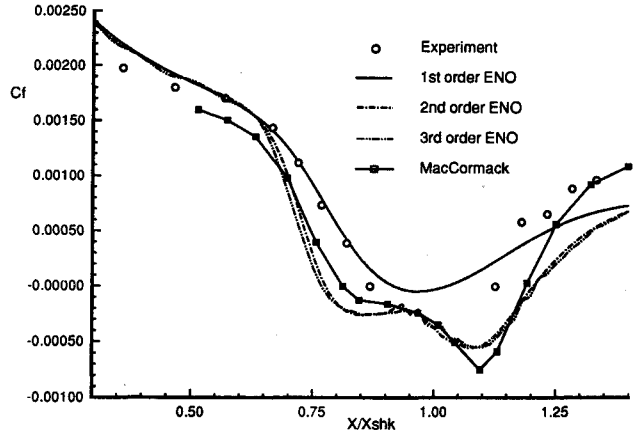

Fig. 6 Skin friction coefficient along plate surface for shock/boundary-layer interaction flow.

The skin friction coefficient defined by $c_f = \tau/(\rho_\infty u_\infty^2/2)$ along the flat plate surface is shown in Fig. 6. The numerical results are compared with the experimental results of Hakkinen et al.[24] and the numerical results of MacCormack.[25] In the present case, the results from the third-order ENO scheme are slightly different than those from the second-order ENO scheme because of the existence of the shock interaction region in the flowfield. The numerical results of the second- and third-order ENO schemes are consistent with MacCormack's results, which were computed with a coarse 32×32 grid and are also consistent with other numerical solutions.[26,27] Note that the experimental results are not available in the separation region because of the limitation of the instrument at the time.[24] The skin friction of the ENO schemes behind the separation region is lower than that of experiment, which is also predicted by other calculations.[26,27] These figures also show that the numerical results of the skin friction distribution obtained by high-order ENO schemes are not very smooth in the separation region because the separation of the boundary layer and the modified ENO reconstruction is used.

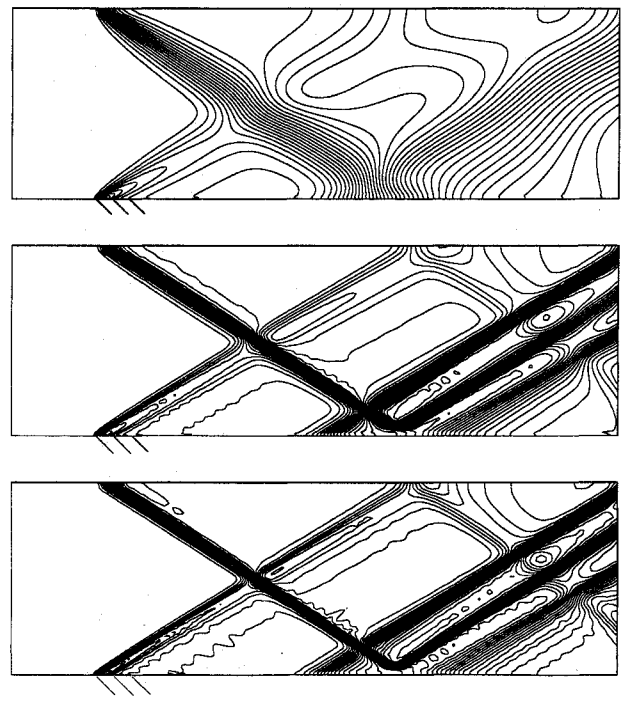

Fig. 7 Pressure contours obtained by using the first-, second-, and third-order ENO schemes with Shu's modification (from top to bottom, respectively).

The pressure contours of three test cases are shown in Fig. 7. The freestream supersonic flow direction is from left to right. The wall is located at the lower surface of the computational domain. A weak shock wave is generated at the leading edge of the plate due to the creation of a boundary layer along the wall surface. The impinging shock from the upper wall interacts with the boundary layer. In the computations, the impinging shock is created as part of the numerical solutions by specifying the flow direction at upper-wall boundary cells behind the impinging shock. This upper-wall boundary condition also creates a reflected shock at the upper wall with the leading-edge shock. This reflected shock does not affect the results of shock-wave/boundary layer interaction on the wall. Figure 7 shows that as the accuracy of the ENO schemes increase, the captured shock waves become more resolved. Meanwhile, the modified ENO schemes tend to be slightly more oscillatory in the interaction area.

The conclusion that can be drawn from these two test cases is that the ENO schemes are able to predict steady viscous flows in

Table 1 Flow conditions for type-IV shock interference heating on a cylinder

Reynolds number, m^{-1}	6.7585×10^6	
Wall temperature, K	294.44	
γ	1.4	
Pr	0.72	
Gas constant, Nm/kg K	286.92	
Cylinder radius, m	0.0381	
Shock angle, deg	18.1114	
Impinging shock location, m	(–0.0889, –0.013276)	
	Freestream	Behind impinging shock
Mach number	8.03	5.25
Temperature, K	111.56	238.04
Pressure, N/m^2	985.01	6996.7
Flow direction, deg	0	12.5

Table 2 Results of grid-refinement study on numerical accuracy

Case	Grids	Stag. heating rates $Q/Q0$	Stag. pressure p/p_0
A	24 × 16	0.88332	0.86011
B	48 × 32	1.3877	0.92596
C	96 × 64	1.0151	0.97683
D	192 × 128	1.0908	0.99202

the boundary layer and with shock-wave/boundary-layer interaction with high resolution. Shu's modified ENO schemes improve the accuracy of the ENO schemes in the boundary-layer computations, and are preferred over the unmodified ENO schemes for the present test cases.

On the other hand, the high-order ENO schemes, which are originally developed for time-accurate computations, have been tested in many time-accurate unsteady problems.[11,12,19,20] For our finite-volume ENO code, we have applied the code to time-accurate computations of two-dimensional hypersonic flow over a flat plate with panel flutter.[28] The time-accurate numerical results of the Euler equations obtained by using the second-order ENO schemes compared very well with the second- and third-order piston theory.

Unsteady Type-IV Shock-Shock Interference Heating

Type-IV shock-shock interference heating on a circular cylinder is computed by using the explicit ENO schemes, which are third-order accurate in time and space, to obtain time-accurate solutions of the Navier-Stokes equations. The test case is chosen to be one of the cases (case S0) of Mach number 8.03 studied by Thareja et al.[5] and the flow conditions are given in Table 1. The results of experimental measurement of pressures and heating rates along a cylinder surface by Wieting and Holden are available for comparison. The flow configuration of type-IV interference heating has been found to be unstable in experimental observations. The inherent unsteadiness of the flowfield is studied in this paper by using high-order ENO schemes so that the time-accurate solutions can be obtained with high resolution.

A CFL number of 0.95 is used in the time-accurate simulation. The gas (air) is assumed to be a perfect gas and viscosity is computed according to Sutherland's Law. A set of body-fitted structured grids (192 ×122) is used in the computations.

The numerical accuracy of the present computations of shock interference heating flow is evaluated by a grid-refinement study on the same hypersonic flow past a cylinder without interference from the impinging shock. The case without interference is used to test the numerical accuracy of the interference-heating-flow solutions because the numerical accuracy mainly depends on the accuracy in resolving the boundary layer. Furthermore, the computational cost of doing a grid-refinement study on the unsteady shock interference flowfield is too high.

The flow conditions and geometry of the grid-refinement study are the same as those given in Table 1 except without the flow condition behind the impinging shock wave. Four sets of grids (cases A–D) are used. The results of the stagnation pressure and heating rates normalized by expected values are shown in Table 2.

The case of the finest grid, case D, has a minimum grid Reynolds number of about 9, and has the same grid size on the cylinder surface as the actual computations for the shock interference flow computations in this paper. Table 2 shows that numerical errors of computing stagnation pressure and heat flux rate are about a few percent for the finest grid, case D.

The time-accurate simulation of the shock-interference flow is carried out as follows. Because the explicit time-accurate computations for the Navier-Stokes equations require extremely small time steps, which are limited by the stability condition, the viscous flow is first computed by using the implicit ENO scheme with a large CFL number. After the boundary layer has settled down, the explicit third-order ENO scheme is used to solve the Navier-Stokes equations for unsteady time-accurate solutions.

The computational results show that the flowfield of the present case of type-IV interference heating computed by the Navier-Stokes equations is inherently unsteady. Figure 8 shows the computational time history of the maximum surface pressure and the location of the maximum pressure measured by the angle from the horizontal position along the cylinder surface. In the plots of this figure, the initial period of time (time < 0.4×10^{-4} s) corresponds to the results of computations using the implicit method; the explicit time-accurate computations start at time ≈ 0.4×10^{-4} s. This figure shows that the flow is oscillatory, as observed by experiments. The dots (#1–#9) on the plots are the instantaneous moments when the flow surface pressure and heat rates are compared

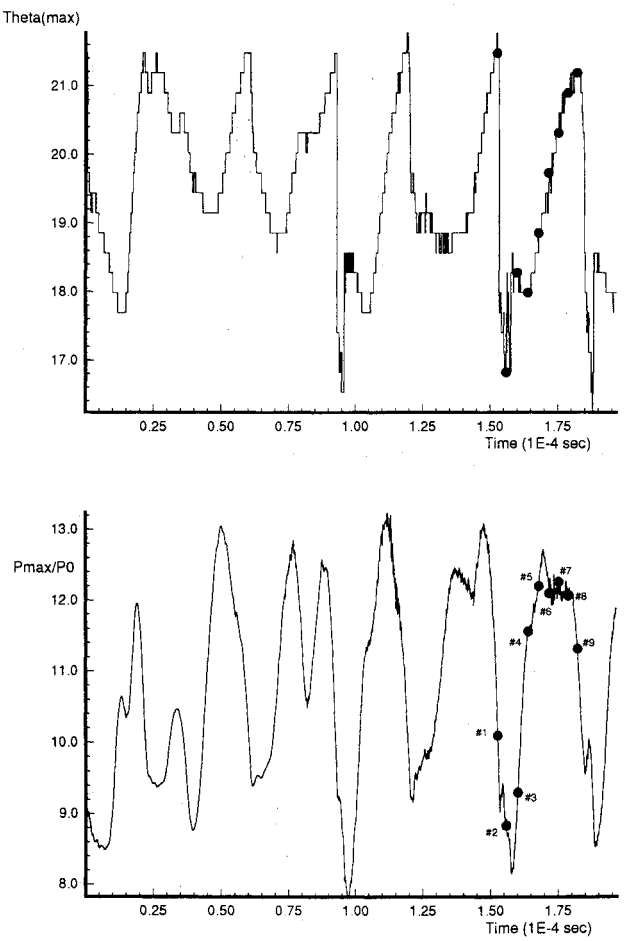

Fig. 8 Time history of maximum surface pressure and its angle on the surface measured from the horizontal position (dots are the moments when the surface parameters and temperature contours are shown in Figs. 8–18).

with experiments and the instantaneous temperature contours are studied. Figure 8 shows that the location of the maximum pressure created by the impinging jet oscillates on the surface within a range of about 3 deg. The maximum surface pressure oscillates by about 33% of the mean value, which shows that the effect of unsteady motion of the flow on surface pressure is significant.

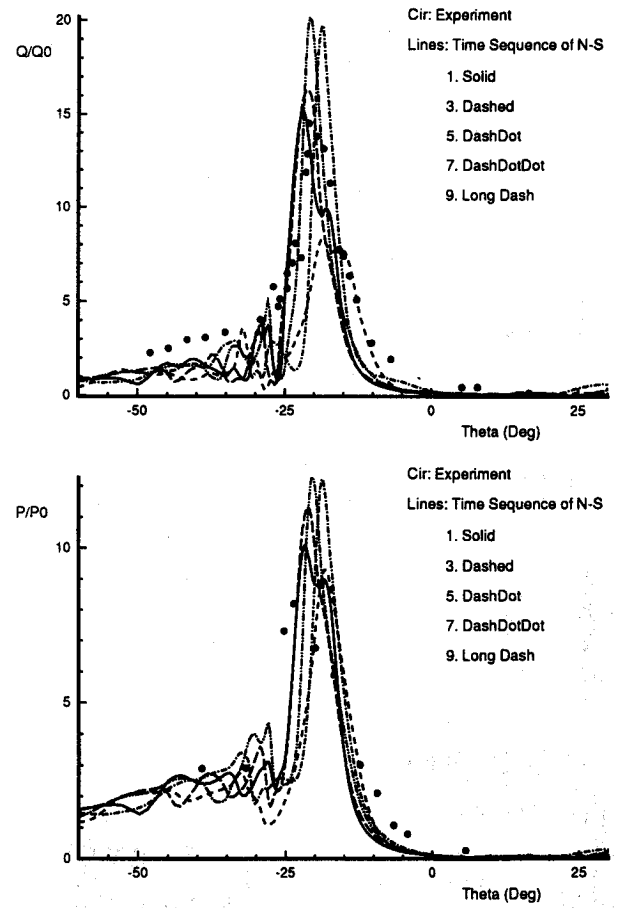

Fig. 9 Instantaneous surface pressure and heat transfer rates for type-IV shock interference flow at $M_\infty = 8.03$ (see Fig. 7 for locations of numbered results in the P_{max}–Time plot).

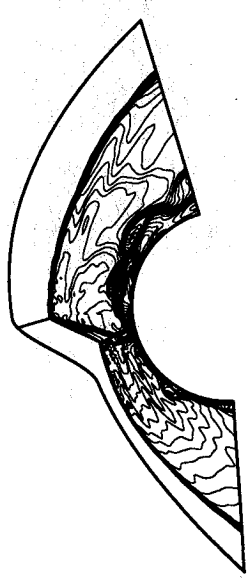

Fig. 10 Temperature contours for the time-accurate Navier-Stokes solutions for type-IV shock interference flow at $M_\infty = 8.03$ (time = 1.958×10^{-4} s).

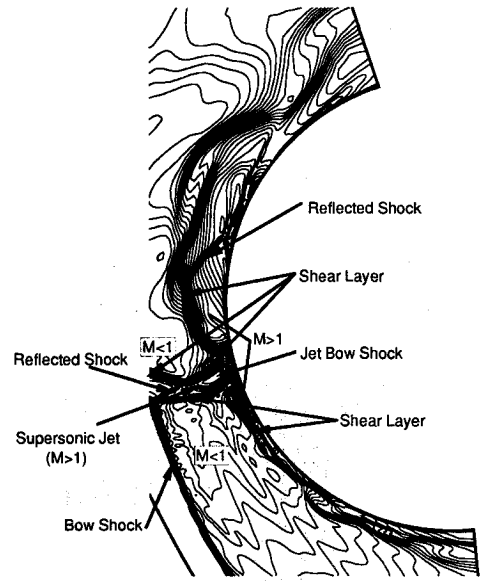

Fig. 11 Flow features shown by the temperature contours for the unsteady type-IV shock interference.

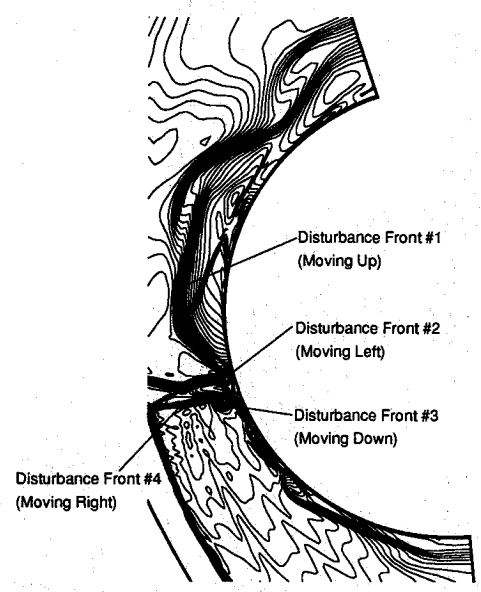

Fig. 12 First of the nine consecutive temperature contours for the unsteady type-IV shock interference, $M_\infty = 8.03$, time = 1.527×10^{-4} s (#1 in Fig. 5).

Figure 9 shows the comparison of instantaneous surface heating rates and surface pressure with experimental results by Wieting and Holden[2] and Thareja et al.[5] The pressure and heat transfer rates along the surface are normalized by the corresponding values of the same freestream without interference heating. For the present test case, there is a difference between the experimental value of the stagnation heating rate for the undisturbed cylinder and the corresponding analytical value.[5] Following the analysis of Thareja et al., we normalize the peak heating rate and surface pressure in Fig. 9 by using the values of noninterference flow, i.e., $Q_0 = 41.43$ Btu/ft^2 s and $p_0/p_\infty = 83.5$. Because the flowfield is unsteady, the experimental results of surface pressure and heating rates are compared with instantaneous numerical results at five consecutive moments of time spanning about one cycle of the oscillations. The locations of these moments of time in the P_{max}–Time plot (#1, #3, #5, #7, and #9) are shown in Fig. 8. Meanwhile, the experimental results are considered to be the average values of the unsteady flowfield. Figure 9 shows that the numerical results

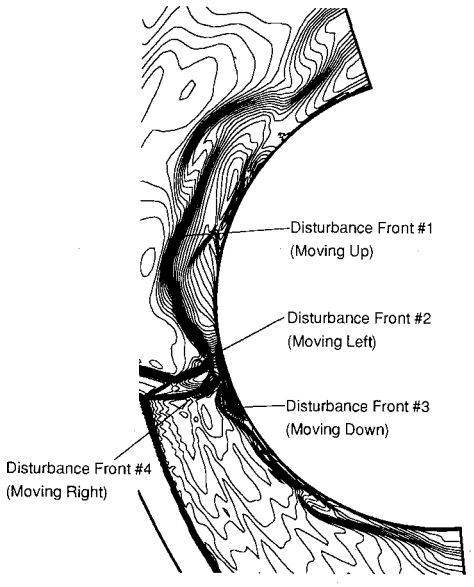

Fig. 13 Third of the nine consecutive temperature contours for the unsteady type-IV shock interference, $M_\infty = 8.03$, time = 1.600×10^{-4} s (#3 in Fig. 7).

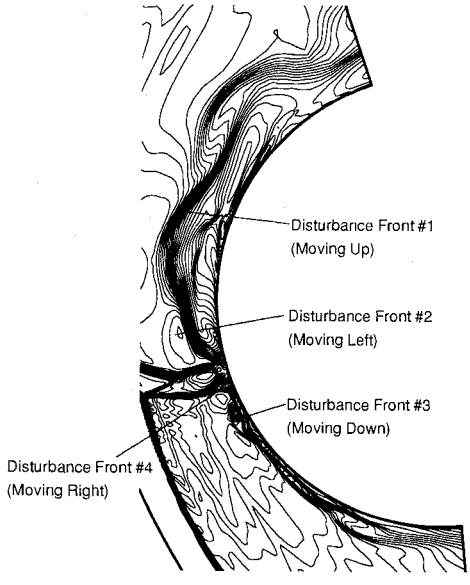

Fig. 14 Fifth of the nine consecutive temperature contours for the unsteady type-IV shock interference, $M_\infty = 8.03$, time = 1.679×10^{-4} s (#5 in Fig. 7).

for surface heating rates compare reasonably well with the experimental results. The numerical results for the surface pressure distribution are slightly higher than the experimental values. The unsteady effect on the surface heating rates is more significant with the maximum heating varying between 8–20 due to the oscillation, which shows that it is important to study the unsteady flowfield with time accuracy to predict the interference heating rates correctly.

On the other hand, the flow pattern and maximum heating rates also depend strongly on the location of the incident shock wave on the main bow shock. The effect of the variation of impingement location on the maximum surface pressure and heat flux were studied by Thareja et al.[5] The present case, S0, corresponds to near-maximum heat amplification due to shock interference among the cases of different shock-impinging locations tested in Ref. 5. In the present computations, the location of the impinging shock is fixed during the computations and the unsteadiness is due to the inherent unsteadiness only. Our results show that the inherent unsteadiness of the interference flow with a fixed impinging location can cause significant oscillations in the maximum heating rates of the cylinder surface. This may explain why the previous steady computations underpredict the heating rates. More studies are needed to understand the unsteady mechanism of the shock interference flow.

The unsteady features of the flowfield and the mechanism of the inherent unsteadiness of the type-IV interference heating flow are more clearly shown by examining the same flowfield temperature contours at consecutive moments of time. Figure 8 shows the locations in the P_{max}–Time plot of five consecutive temperature contours (#1, #3, #5, #7, and #9) which will be shown in Figs. 12–16. These five contours span approximately one cycle of the oscillation in the unsteady motion of the interference flowfield with a frequency of roughly 30 KHz. Because the temperature distributions in the flowfield have steep jumps across the shock waves and across the shear layers, the temperature contours are most suitable to show the unsteady interaction of the type-IV interference flowfield.

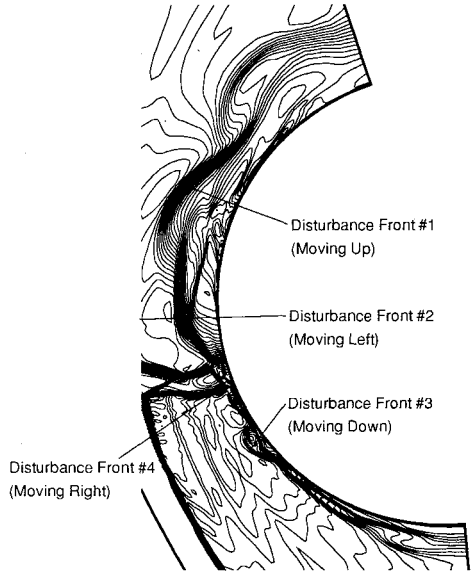

Fig. 15 Seventh of the nine consecutive temperature contours for the unsteady type-IV shock interference, $M_\infty = 8.03$, time = 1.753×10^{-4} s (#7 in Fig. 7).

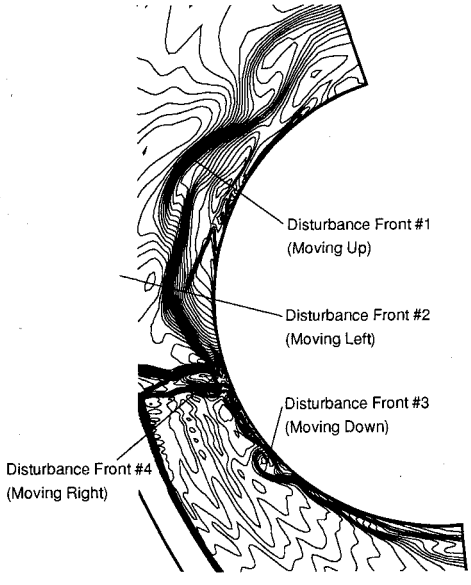

Fig. 16 Ninth of the nine consecutive temperature contours for the unsteady type-IV shock interference, $M_\infty = 8.03$, time = 1.822×10^{-4} s (#9 in Fig. 7).

The temperature contours of the whole flowfield at the moment of time = 1.958×10^{-4} s are shown in Fig. 10. (See Fig. 8 for the locations in the P_{max}–Time plot.) To focus on the unsteady oscillation in the impinging region, the temperature contours in a smaller local area near the impinging point are plotted in Figs. 11–16. Figure 11 shows the basic unsteady flow features near the interference region shown by the temperature contours. The unsteady flow interaction among the supersonic jet, jet bow shock, the shear layers, and the upstream bow shocks can be studied from the temperature contours.

The zoomed temperature contours at consecutive moments of time with 1000 time steps between each set of contours are shown in Figs. 12–16. The unsteady mechanism can be observed in the numerical solutions of these temperature contours. In these figures, the interaction can be studied by tracking four disturbance fronts that are marked on the figures. Disturbance front #3 is the disturbance created by the impinging jet bow shock to the lower shear layer along the surface. The consecutive figures show that this disturbance front travels along the shear layer downstream through a shear-layer instability. Similarly, disturbance front #1 is the disturbance to the upper shear layer and travels up along the surface downstream through the shear-layer instability. Disturbance fronts #2 and #4 are weak disturbance fronts traveling along the shear layers above and below the supersonic jet. The figures show that disturbance front #2 propagates left toward the upstream bow shock through the subsonic region above the jet. On the other hand, disturbance front #4 propagates right through the shear layer below the supersonic jet toward the jet bow shock on the surface.

The propagation of these disturbance fronts clearly shows the feedback mechanism behind the inherent unsteadiness of the shock interference flowfield. The impinging jet bow shock wave oscillates up and down. This unsteady up-down motion of the supersonic jet impinging point creates two shear-layer instabilities in the two branches of shear layers along the cylinder surface. The disturbance of shear-layer instability propagates along the shear layers downstream (disturbance front #3 and #1). Because the regions between the freestream bow shocks and the shear layers are subsonic, the disturbance propagates back to the upstream bow shocks along the upper shear layer above the supersonic jet (disturbance front #2). This disturbance causes the unsteadiness of the upstream bow shocks. In turn the disturbance of the upstream bow shocks propagates along the lower shear layer (disturbance front #4) back to the jet impinging point on the surface. This disturbance will cause new oscillations in the jet and the jet bow shock. Therefore, the shear-layer instabilities, the bow shock, and the supersonic jet form a limit cycle of a feedback system through the subsonic flow region behind the freestream bow shock. As a result, the flow is inherently unstable even when the freestream flow conditions are constant.

It should be pointed out that the preceding analysis of the unsteady mechanism is based on the observation of the numerical results only; more theoretical and numerical studies are needed to understand the unsteady mechanism, which is important for the prediction of interference heating problems.

Conclusions

The high-order, finite-volume, essentially nonoscillatory (ENO) schemes have been used to obtain time-accurate solutions of the Navier-Stokes equations to study the unsteady hypersonic shock-shock interference heating on a cylinder. High-resolution numerical solutions of the Navier-Stokes equations for unsteady type-IV hypersonic shock-shock interfence heating problems have been obtained. The inherent unsteadiness of the flow is captured with high resolution by the third-order accurate ENO schemes. The results show that the inherent unsteadiness is the result of the interaction among the unsteady shear layers and the bow shocks. The numerical results of the surface heating rates and pressure agree reasonably well with experimental results.

Meanwhile, implicit ENO schemes for solving the Navier-Stokes equations have been applied to test cases of steady high-Reynolds-number viscous flows. The test cases include supersonic boundary layer and shock/boundary-layer interaction flows. The results show that steady-state solutions of viscous flows can be obtained efficiently by using the implicit two-dimensional ENO schemes, and that higher order accurate ENO schemes lead to better resolution in the shock waves and the boundary layers.

Acknowledgments

This research was supported by the Air Force Office of Scientific Research Grant F49620-92-J-0090 P00001 monitored by Len Sakell. The author would like to thank the reviewers for their constructive comments.

References

[1]Edney, B., "Anomalous Heat Transfer and Pressure Distributions on Blunt Bodies at Hypersonic Speeds in the Presence of an Impinging Shock," Aeronautical Research Inst. of Sweden, FFA Rept. 115, Feb. 1968.

[2]Wieting, A. R., and Holden, M. S., "Experimental Shock-Wave Interference Heating on a Cylinder at Mach 6 and 8," *AIAA Journal*, Vol. 27, No. 11, 1989, pp. 1557–1565.

[3]Holden, M. S., "Shock-Shock Boundary Layer Interaction," AGARD, Rept. No. 764, July 1989.

[4]Klopfer, G. H., and Yee, H. C., "Viscous Hypersonic Shock-on-Shock Interaction on Blunt Cowl Lips," AIAA Paper 88-0233, Jan. 1988.

[5]Thareja, R. R., Stewart, J. R., Hassan, O., Morgan, K., and Peraire, J., "A Point Implicit Unstructured Grid Solver for the Euler and Navier-Stokes Equations," *International Journal for Numerical Methods in Fluids*, Vol. 9, No. 4, 1989, pp. 405–425.

[6]Gaitonde, D., and Shang, J. S., "The Performance of Flux-Split Algorithms in High-Speed Viscous Flows," AIAA Paper 92-0186, Jan. 1992.

[7]Tannehill, J. C., Holst, T. L., and Rakich, J. V., "Numerical Computation of Two-Dimensional Viscous Blunt Body Flows with an Impinging Shock," *AIAA Journal*, Vol. 14, No. 2, 1976, pp. 204–211.

[8]Tannehill, J. C., Holst, T. L., Rakich, J. V., and Keyes, J. W., "Comparison of a Two-Dimensional Shock Impingement Computation with Experiment," *AIAA Journal*, Vol. 14, No. 4, 1976, pp. 539–541.

[9]Tannehill, J. C., Vigneron, Y. C., and Rakich, J. V., "Numerical Solution of Two-Dimensional Turbulent Blunt Body Flows with an Impinging Shock," *AIAA Journal*, Vol. 17, No. 12, 1979, pp. 1289, 1290.

[10]Harten, A., "High Resolution Schemes for Hyperbolic Conservation Laws," *Journal of Computational Physics*, Vol. 49, No. 3, 1983, pp. 357–393.

[11]Harten, A., Engquist, B., Osher, S., and Chakravarthy, S., "Uniformly High Order Accurate Essentially Non-Oscillatory Schemes, III," *Journal of Computational Physics*, Vol. 71, No. 2, 1987, pp. 231–303.

[12]Casper, J., "Essentially Non-Oscillatory Shock Capturing Schemes to Multi-Dimensional Systems of Conservation Laws" Ph.D. Thesis, Old Dominion Univ., Norfolk, VA, Dec. 1990.

[13]Yang, J. Y., "Third-Order Nonoscillatory Schemes for the Euler Equations," AIAA Paper 90-0110, 1990.

[14]Barth, T. J., and Frederickson, P. O., "Higher Order Solution of the Euler Equations on Unstructured Grids Using Quadratic Reconstruction," AIAA Paper 90-0013, Jan. 1990.

[15]Shu, C.-W., Erlebacher, G., Zang, T. A., Whitaker, D., and Osher, S., "High-Order ENO Schemes Applied to Two- and Three-Dimensional Compressible Flow," Computational and Applied Mathematics, Dept. of Mathematics, Univ. of California, Los Angeles, Rept. 91-09, Los Angeles, CA, 1991.

[16]Atkins, H. L., "High-Order Essentially Nonoscillatory Methods for the Unsteady Compressible Navier-Stokes Equations," AIAA Paper 91-1557, June 1991.

[17]Roe, P. L., "Approximate Riemann Solvers, Parameter Vectors and Difference Schemes," *Journal of Computational Physics*, Vol. 43, No. 2, 1981, pp. 357–372.

[18]Rogerson, A. M., and Meiburg, E., "A Numerical Study of the Convergence Properties of ENO Schemes," *Journal of Scientific Computing*, Vol. 5, No. 2, June 1990, pp. 151–167.

[19]Shu, C.-W., "Numerical Experiments on the Accuracy of ENO and Modified ENO Schemes," *Journal of Scientific Computing*, Vol. 5, No. 2, 1990, pp. 127–149.

[20]Shu, C.-W., and Osher, S., "Efficient Implementation of Essentially Non-Oscillatory Schemes," ICASE Rept. No. CR 87-33, NASA, May 1987.

[21]MacCormack, R. W., "Current Status of Numerical Solution of the Navier-Stokes Equations," AIAA Paper 85-0032, Jan. 1985.

[22]Casper, J., "Finite Volume Implementation of High-Order Essentially Nonoscillatory Schemes in Two-Dimensions," *AIAA Journal*, Vol. 30, No.

12, 1992, pp. 2829–2835.
[23]Lawrence, S. L., Tannehill, J. C., and Chausee, D. S., "Upwind Algorithm for the Parabolized Navier-Stokes Equations," *AIAA Journal*, Vol. 27, No. 9, 1989, pp. 1175–1183.
[24]Hakkinen, R. J., Greber, I., Trilling, L., and Abarbanel, S. S., "The Interaction of an Oblique Shock Wave with a Laminar Boundary Layer," NASA Memo 2-18-59W, 1959.
[25]MacCormack, R. W., "A Numerical Method for Solving the Equations of Compressible Viscous Flow," *AIAA Journal*, Vol. 20, No. 9, 1982, pp. 1275–1281.
[26]Wang, Z., and Richards, B. E., "High Resolution Schemes for Steady Flow Computation," *Journal of Computational Physics*, Vol. 97, No. 1, 1991, pp. 53–72.
[27]Katzer, E., "Laminar Shock/Boundary-Layer Interaction—A Numerical Test Problem," *Numerical Treatment of the Navier-Stokes Equations*, edited by W. Hackbusch and R. Rannacher, Vieweg, Braunschweig, Germany, 1990, pp. 82–89.
[28]Bein, T., Friedmann, P., Zhong, X., and Nydick, I., "Hypersonic Flutter of a Curved Shallow Panel with Aerodynamic Heating," AIAA Paper 93-1318, April 1993.